# A Unified Approach for the Commissioning of Synchronous Reluctance Motor Drives

Andrea Credo, Francesco Parasiliti, Marco Tursini *Member, IEEE*, and Marco Villani

***Abstract*—This paper presents a unified procedure for commissioning synchronous reluctance motor drives based on a fast sequence of targeted feedings using the drive inverter.**

**The method requires measuring the values of the phase currents and their derivatives by time-based samplings with still rotor and subsequent model-based computations. It allows the self-evaluation of the phase resistance and the d-q axes inductances for the pre-set of the field-oriented current regulators. Moreover, it detects the rotor position without movement, a functionality needed at start-up for motors equipped with incremental encoders in the standard service.**

**The study refers to a 3kW synchronous reluctance motor prototype with a flux barrier rotor. Both realistic simulations accounting for the non-linear machine behavior and experimental tests are presented, showing the error between the estimated position, the phase resistance, and the d-q axes inductances and the effective ones. The results prove the reliability of the method.**

***Index Terms*— Co-simulation, fast commissioning, finite elements modeling, inductance estimation, initial position estimation, synchronous reluctance motor, resistance estimation.**

## NOMENCLATURE

| | |
|---|---|
| $d$-$q$ | Rotor axes with the minimum (d) and maximum (q) reluctance |
| $I_a, I_b, I_c$ | Phase currents of the motor |
| $L_{aa}$,$L_{bb}, L_{cc}$ | Self-inductances of each phase |
| $L_{ab}$,$L_{bc}, L_{ca}$ $L_{ba}$,$L_{cb}, L_{ac}$ | Mutual-inductances between two phases |
| $L_{\sigma s}$ | Leakage inductance |
| $L_d, L_q$ | Direct and quadrature axis inductance |
| $L_{\mu s}$ | Constant component of phase inductance |
| $L_{\Delta s}$ | Amplitude of the 2nd-harmonic component of phase inductance |
| $R_s$ | Phase resistance |
| $V_a, V_b, V_c$ | Phase voltages of the motor |
| $V_{dc}$ | DC bus voltage |
| $x, y, z, A$ | Coefficients useful for the calculation |
| $\theta_r$ | Electric rotor position |
| $\varphi_a, \varphi_b, \varphi_c$ | Phase fluxes of the motor |

Andrea Credo, Francesco Parasiliti, Marco Tursini, and Marco Villani are with the Department of Industrial and Information Engineering and Economics, University of L'Aquila, L'Aquila 67100, Italy (e-mail: Andrea.Credo@univaq.it, Francesco.Parasiliti@univaq.it, Marco.Tursini@univaq.it, Marco.Villani@univaq.it).

## I. INTRODUCTION

THE Synchronous Reluctance (SynRel) motor is becoming a serious alternative to Permanent Magnets (PM) motors in high-performance mass applications because of the instability of the market of rare earth magnets in the last decade [1]-[7].

Compared to PM motors, the disadvantages attributed to the SynRels are the lower performance and the higher complexity of the control. But nowadays, Finite Elements (FE) design tools combined with sophisticated optimization algorithms allow for performance very close to that of PM motors of the same size [8]-[12]. And research proceeds to develop control strategies workable, although there is not yet a consolidated approach [13]-[14]. The control complexity of the SynRels is due to the non-linearity of the torque-to-current ratio and flux-current relation. Flux-oriented control allows for maximum performance, but identification of specific characteristics and parameters of each machine is needed, namely a solution for commissioning [15]-[16].

Various identification methods have been proposed for SynRels motors based on design data and/or experiments [17]. The Finite Element Analysis (FEA) allows for computing parameters and control characteristics by design data. But these last are typically protected and only accessible by the motor designer and producer. Moreover, not-trivial tests are needed on the actual machine to confirm the computation accuracy. For these reasons, this method is often impractical.

Experimental identification solves the uncertainties related to the manufacturing process. Most of the methods proposed for SynRels are based on magnetic salience and follow solutions adopted for the interior PM motors. The knowledge of the rotor position is needed in salient machines because the $d$ and $q$-axis inductances are different. Dutta [18] and Jabbar [19] propose adopting artificial intelligence techniques to estimate the flux-current relationship during offline sinusoidal supply. These techniques require additional instrumentation, lab resources, and a lot of time for evaluation.

Depending on whether the motor is mechanically joined to the load, it is common to distinguish between "load-on-line" or "load-off-line" identification methods.

Load-off-line methods allow for the rotor movement (alignment) toward those fixed stator positions useful to measure the $d$-$q$ inductances. In this case, the identification process does not need the position information and can be carried out apart from the presence of a position sensor.

On the other hand, alignment movements are not always

possible for relevant load-on-line applications. That is the case with elevators and electric vehicles (where uncontrolled rotor movement is not allowed) or fans and pumps (where rotor movement in only one direction is recommended). If the position sensor is an incremental encoder in such applications, the initial rotor position is unknown, precluding any identification possibility at drive start-up. Hence, estimating the rotor position becomes the first step of the identification process, needed for commissioning and, later, in the standard service for field orientation [20].

Many works in the literature refer to the estimation of the initial rotor position for the PM motors, both surface [21]-[23] and interior types [24]-[27]. The topic is also addressed for the Switched Reluctance Motor (SRM) in [28]-[30], while specific proposals for the SynRel are missing from the authors' knowledge.

Several of these works investigate the initial rotor position estimation with pulse voltage injection method [20]-[22], [29] or high-frequency rotating voltage signal injection method [23], or high-frequency injection methods [24]-[26].

In [27], a particular supply voltage pattern is used to compute the phase inductances, which depends on the position of the rotor. Then the initial rotor position is calculated according to the identified values of the phase inductances. The method is valid but requires a feeding sequence of about 100 ms for its computation. Moreover, the rotor position could change during this time, both for the currents applied and for an external torque.

In [28], a neural network method is proposed and discussed for an SRM motor. It is based on the knowledge of the flux characteristics of the machine, then adopts a back-propagation neural network (BPNN) with an improved algorithm and radial basis function neural network (RBFNN) to build an SRM rotor position model. This method requires a FEM model for learning the neural network or a collection of flux data measurements.

The high-frequency signal-injection techniques developed for sensorless control presented in [31]-[33] allow initial rotor position estimation, but they are not helpful for parameter estimation. The initial rotor position can be also evaluated with AC signal with same flux observer used for FOC aided by active flux concepts [34]-[35]. As described in [36], the cross-coupling saturation affects the position estimation in injection-based sensorless control algorithms for SynRels.

In [37], the offline commissioning of Permanent Magnet Synchronous Motor (PMSM) is proposed with an external power analyzer. The method is used to perform the torque estimation, a critical value in several applications.

The procedure for the commissioning of induction motors is discussed in [38]-[40], which adopt a model-based observer to estimate rotor and stator parameters.

The fast commissioning of the SynRel motor is addressed in [41]-[43]. These works concern the model-free predictive current control, a solution that makes it difficult to achieve an optimized control such as the Maximum Torque Per Ampere (MTPA).

This work presents a full procedure for fast commissioning SynRel motor drives, extending the authors' research in [1]. The method estimates the initial rotor position, the phase resistance, and the *d-q* axes inductances at a rotor standstill exploiting the magnetic saliency of the machine. Detection of the initial rotor position requires measuring the values of the phase currents and their derivatives by a particular sequence of supply voltages. Compared to the previous study [1], this work includes estimating the phase resistance and axis inductances and extends the experimental results accordingly. Estimation of such parameters is an essential requirement for the optimum design of the PI current regulators, one of the primary goals of a commissioning procedure. Basic guidelines on this matter are also given.

Compared to other papers which discuss the adoption of position estimation in injection-based sensorless control, the proposed method is applied when the control is disabled; therefore, it is possible to avoid deep magnetic saturation in the machine leading to a simplification of the estimation of initial position, axis inductances, and phase resistance.

This procedure can be combined with a sensorless algorithm in order to allow encoderless control. If signal injections techniques are adopted, the discussed method can be used for the inductances and resistance estimation for PI tuning, and the position (also the initial one) is obtained with more sophisticated algorithms; if a flux observer is involved, it requires the initial position (computed with the method) for better commissioning in the first instants.

The paper is organized as follows: Section II describes the SynRel flux and voltage models, and Section III illustrates the ideas and the methodology underlying the estimation of the initial position, the phase resistance, and the axis inductances. Section IV discusses the possible nonlinearities that could affect the proposed methodology and Section V presents the application of this technique to an industrial SynRel through a Finite Element (FE) co-simulation to evaluate the behavior of the currents and their derivatives and the quality of the presented method. The experimental validation is presented in Section VI and, finally, Section VII presents and discusses the conclusions.

Fig. 1 summarizes the proposed commissioning procedure.

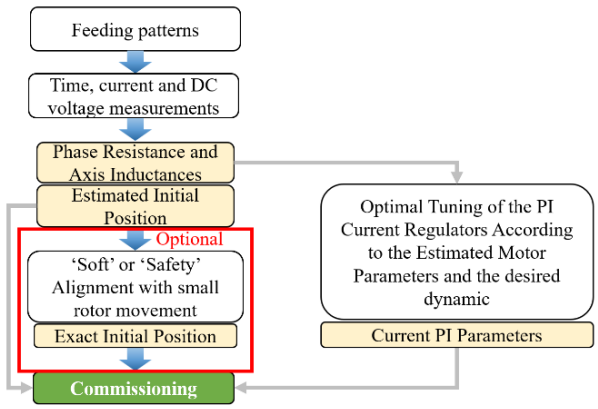


**Fig. 1.** Proposed flow diagram for the commissioning of the SynRel.

## II. Flux and Voltage Models

The technique developed in this work takes its operating principle from the well-known expressions of self and mutual inductances, flux linkages, and phase voltages for a SynRel, as shown in the appendix.

The followings resume the simplifying hypotheses implied in the above model.

1st, variations of the phase inductances due to saturation are neglected. Particularly both the constant component ($L_{\mu s}$) of the phase inductances (due to the magnetization) and the amplitude of the 2nd-harmonic component $L_{\Delta s}$ (due to the anisotropy) are assumed to be equal to the respective un-saturated values. If the equivalent $d$-current during the considered feeding patterns is lower than the one which occurs at the saturation condition, this simplification correctly represents the machine's behavior. In particular, the estimated inductance will be lower than the saturated one, and the computed value can be used for designing the PI regulator with a minimum performance difference. Furthermore, the unsaturated inductance values correctly represent the machine in a large working area, and their consideration does not affect the position estimation.

2nd, high-order harmonics in phase inductances are neglected. Actually, the inductances (due to the magnetization and anisotropy) are also a function of the rotor position because of the higher-order flux (inductance) harmonics. This effect is assumed to deteriorate the accuracy of the proposed estimation method, given that the feeding patterns exploit different rotor angles.

Based on what has just been stated and considering that the procedure is carried out at standstill, the voltage equations can be written as follows:

$$\begin{aligned} V_a = R_s I_a &+ \left[L_{\sigma s} + L_{\mu s} + L_{\Delta s}\cos(2\theta_r)\right]\frac{dI_a}{dt} \\ &+ \left[-\frac{1}{2}L_{\mu s} + L_{\Delta s}\cos\left(2\theta_r - \frac{2}{3}\pi\right)\right]\frac{dI_b}{dt} \\ &+ \left[-\frac{1}{2}L_{\mu s} + L_{\Delta s}\cos\left(2\theta_r + \frac{2}{3}\pi\right)\right]\frac{dI_c}{dt} \end{aligned} \quad (1)$$

$$\begin{aligned} V_b = R_s I_b &+ \left[-\frac{1}{2}L_{\mu s} + L_{\Delta s}\cos\left(2\theta_r - \frac{2}{3}\pi\right)\right]\frac{dI_a}{dt} \\ &+ \left[L_{\sigma s} + L_{\mu s} + L_{\Delta s}\cos\left(2\theta_r + \frac{2}{3}\pi\right)\right]\frac{dI_b}{dt} \\ &+ \left[-\frac{1}{2}L_{\mu s} + L_{\Delta s}\cos(2\theta_r)\right]\frac{dI_c}{dt} \end{aligned} \quad (2)$$

$$\begin{aligned} V_c = R_s I_c &+ \left[-\frac{1}{2}L_{\mu s} + L_{\Delta s}\cos\left(2\theta_r + \frac{2}{3}\pi\right)\right]\frac{dI_a}{dt} \\ &+ \left[-\frac{1}{2}L_{\mu s} + L_{\Delta s}\cos(2\theta_r)\right]\frac{dI_b}{dt} \\ &+ \left[L_{\sigma s} + L_{\mu s} + L_{\Delta s}\cos\left(2\theta_r - \frac{2}{3}\pi\right)\right]\frac{dI_c}{dt} \end{aligned} \quad (3)$$

## III. Estimation Procedure

Suppose that an inverter feeds the stator windings of the reluctance motor. The estimation procedure is based on a two-step sequence. In the first step (Fig. 2), only the phases "$a$" and "$b$" are fed, while phase "$c$" is open (feeding pattern "$a$-$b$"). Since the motor phases are star-connected, the phase "$a$" current and its derivative have the same value as the phase "$b$" current and its derivative, but with the opposite sign, and the phase "$c$" current is zero. The following expressions describe the above conditions:

$$I_c = 0;\ \frac{dI_c}{dt} = 0;\ I_b = -I_a;\ \frac{dI_b}{dt} = -\frac{dI_a}{dt} \quad (4)$$

Fig. 3 shows the current path in the second step when all the commands are set to 0. The power supply to phases "$a$" and "$b$" is removed, and the energy stored in the inductance is provided to the DC capacitor if the DC power source is unidirectional, as supposed in the simulation results (Section VI) and used in the experimental setup (Section VII).

Then the sequence is repeated to fed phases "$b$" and "$c$" (Fig. 4, feeding pattern "$b$-$c$") and phases "$c$" and "$a$" (Fig. 5, feeding pattern "$c$-$a$").

The adopted model correctly represents the machine if the saturation is not reached. Because it is not possible to know a priori what is the saturation condition, it is possible to select during the feeding pattern a time window in which the current is quite linear. In this condition, the inductance is constant and under the saturation level. Therefore, even if the saturation could be reached during the procedure, these data can be neglected in post-processing for position and inductance computation.

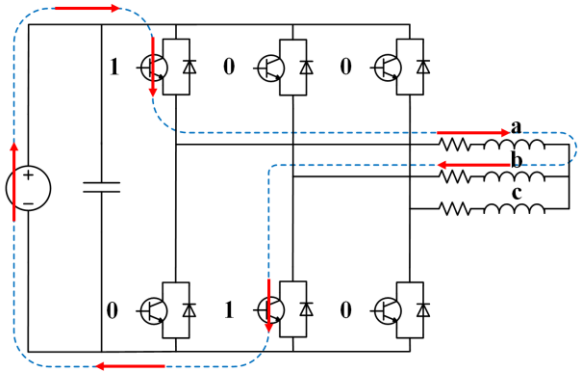


**Fig. 2.** Step 1: energization of "a" and "b" phases and resultant current path.

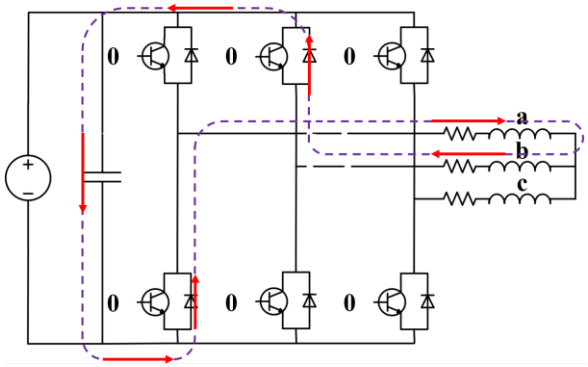


**Fig. 3.** Step 2: de-energization of phases of "a" and "b" and resultant current path.

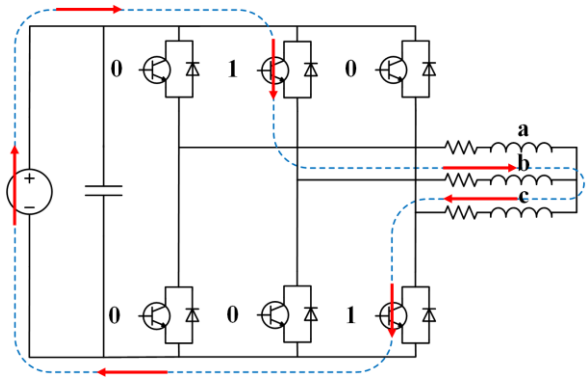


**Fig. 4.** Energization of "b" and "c" phases and resultant current path.

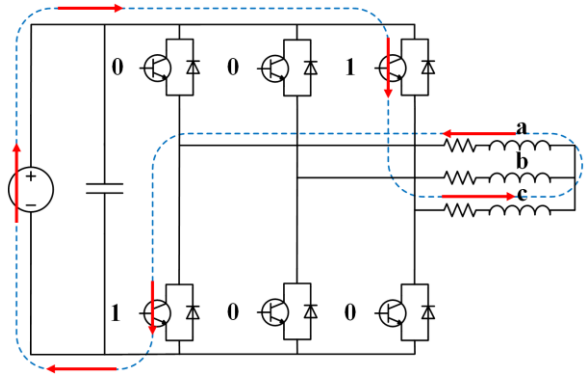


**Fig. 5.** Energization of "c" and "a" phases and resultant current path.

*A. Phase Resistance Estimation*

The estimation procedure starts with the computation of the phase resistance. During the energization step, considering a generic time interval $t_1$, the current $I_{a,1}(t_1)$ flowing through phases "$a$" and "$b$" can be obtained as the expression of the current in an RL circuit fed by a constant DC voltage:

$$I_{a,1}(t_1) = \frac{V_{dc}}{2R_s}\left(1 - e^{-\frac{t_1}{\tau}}\right) + I_{a,1}(0)e^{-\frac{t_1}{\tau}} \tag{5}$$

where $I_{a,1}(0)$ is the value of the current at the considered time zero, $t_1$ is the generic time interval for the computation during the step 1, $\tau = L/(2R_s)$ is the time constant of the circuit, and $L$ is the value of the sum of the inductances of the phase "$a$" and "$b$".

During the de-energization step (in which the value of the constant DC voltage is negative, as shown in Fig. 3), considering a generic time interval $t_2$, the current $I_{a,2}(t_2)$ flowing through phases "$a$" and "$b$" has the following expression:

$$I_{a,2}(t_2) = -\frac{V_{dc}}{2R_s}\left(1 - e^{-\frac{t_2}{\tau}}\right) + I_{a,2}(0)e^{-\frac{t_2}{\tau}} \tag{6}$$

where $I_{a,2}(0)$ is the value of current at the considered time zero and $t_2$ is the generic time interval for the computation during de-energization.

Summing the equations (5) and (6) and considering the same time interval for the steps 1 and 2 ($t_1 = t_2 = t^*$), as shown in Fig. 6, it is possible to write the following expressions:

$$I_{a,1}(t^*) + I_{a,2}(t^*) = \frac{V_{dc}}{2R_s}\left(1 - e^{-\frac{t^*}{\tau}}\right) + I_{a,1}(0)e^{-\frac{t^*}{\tau}} - \frac{V_{dc}}{2R_s}\left(1 - e^{-\frac{t^*}{\tau}}\right) + I_{a,2}(0)e^{-\frac{t^*}{\tau}} \tag{7}$$

$$I_{a,1}(t^*) + I_{a,2}(t^*) = \left[I_{a,1}(0) + I_{a,2}(0)\right]e^{-\frac{t^*}{\tau}} \tag{8}$$

$$\tau = -\frac{t^*}{\log\left[\frac{I_{a,1}(t^*) + I_{a,2}(t^*)}{I_{a,1}(0) + I_{a,2}(0)}\right]} \tag{9}$$

$$R_s = \frac{V_{dc}}{2\left[I_{a,1}(t^*) - I_{a,1}(0)e^{-\frac{t^*}{\tau}}\right]}\left(1 - e^{-\frac{t^*}{\tau}}\right) \tag{10}$$

As regard to phase resistance computation, it is possible to use any time interval and any time zero for steps 1 and 2. A proper choice (the one adopted in this paper) is to fix the time interval ($t^*$) to have a good number of samples and to select for the first interval the time zero so that it ends with the final time of step 1. The time zero of the second interval is selected equal to the beginning of step 2. With this choice, the terms $I_{a,1}(t^*)$ and $I_{a,2}(0)$ are equal, as shown in Fig. 7.

The resistance calculation can be repeated by applying the same sequence to the pair of phases "$b$" and "$c$" (Fig. 4) and then to the pair "$c$" and "$a$" (Fig. 5), finally averaging the three values obtained, for a better result. In this way, it is possible to reduce the measurement error during the procedure. The proposed method for phase resistance computation neglects the nonlinear effects of the inverter, which are critical at small quantities of voltage. This should not affect the results because, during the proposed procedure, the motor is fed with the maximum available DC voltage, which is much higher than the nonlinear voltage drop of the inverter.

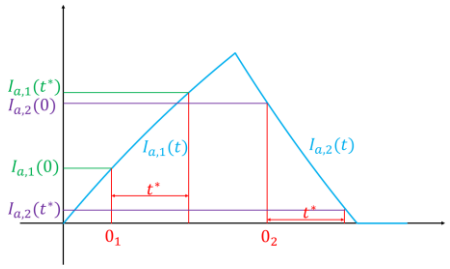


**Fig. 6.** Current behavior during the feeding sequence considering the same time interval between the samples in step 1 (energization) and step 2 (de-energization).

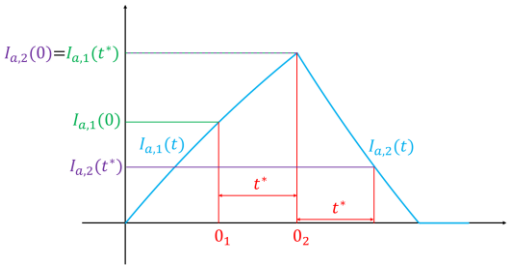


**Fig. 7.** Same as Fig. 6 with 2nd current sample of step 1 equal to the 1st sample of step 2.

*B. Rotor Position Estimation*

Based on expressions (4), it is possible to write the simplified expression of the voltage between the phases "$a$" and "$b$":

$$V_{ab} = V_{dc} = L_{\Delta s}\left[\cos(2\theta_r) - 2\cos\left(2\theta_r - \frac{2}{3}\pi\right) + \cos\left(2\theta_r + \frac{2}{3}\pi\right)\right]\frac{dI_{a,1}}{dt} + 2R_s I_{a,1} + 2\left(L_{\sigma s} + \frac{3}{2}L_{\mu s}\right)\frac{dI_{a,1}}{dt} \quad (11)$$

Analogous expressions can be obtained for the voltage $V_{bc}$ relating to the feeding pattern "$b$-$c$", and $V_{ca}$, relating to the feeding pattern "$c$-$a$". The trigonometric manipulation of the above expressions leads to the following equations:

$$V_{dc} = 2R_s I_{a,1} + \left[2\left(L_{\sigma s} + \frac{3}{2}L_{\mu s}\right) - 3L_{\Delta s}\cos\left(2\theta_r - \frac{2}{3}\pi\right)\right]\frac{dI_{a,1}}{dt} \quad (12)$$

$$V_{dc} = 2R_s I_{b,1} + \left[2\left(L_{\sigma s} + \frac{3}{2}L_{\mu s}\right) - 3L_{\Delta s}\cos(2\theta_r)\right]\frac{dI_{b,1}}{dt} \quad (13)$$

$$V_{dc} = 2R_s I_{c,1} + \left[2\left(L_{\sigma s} + \frac{3}{2}L_{\mu s}\right) - 3L_{\Delta s}\cos\left(2\theta_r + \frac{2}{3}\pi\right)\right]\frac{dI_{c,1}}{dt} \quad (14)$$

where only the rotor position and the leakage, the constant component, and the 2nd-harmonic component of phase inductance are unknown because the DC voltage is known, the phase current and its derivative are measured, and the phase resistance is computed by (10).

Calculating the rotor position can be facilitated by compacting relations (12)-(14) as follows:

$$x = \left[A - 3L_{\Delta s}\cos\left(2\theta_r - \frac{2}{3}\pi\right)\right] = \frac{V_{dc} - 2R_s I_{a,1}}{\frac{dI_{a,1}}{dt}} \quad (15)$$

$$y = [A - 3L_{\Delta s}\cos(2\theta_r)] = \frac{V_{dc} - 2R_s I_{b,1}}{\frac{dI_{b,1}}{dt}} \quad (16)$$

$$z = \left[A - 3L_{\Delta s}\cos\left(2\theta_r + \frac{2}{3}\pi\right)\right] = \frac{V_{dc} - 2R_s I_{c,1}}{\frac{dI_{c,1}}{dt}} \quad (17)$$

being:

$$A = 2\left(L_{\sigma s} + \frac{3}{2}L_{\mu s}\right) = \frac{x + y + z}{3} \quad (18)$$

By manipulating the previous equations, it is possible to write:

$$x - y = 3L_{\Delta s}\left[\cos(2\theta_r) - \cos\left(2\theta_r - \frac{2}{3}\pi\right)\right] = 3L_{\Delta s}\left[-2\sin\left(2\theta_r - \frac{\pi}{3}\right)\sin\left(\frac{\pi}{3}\right)\right] \quad (19)$$

$$x - y = -3\sqrt{3}L_{\Delta s}\sin\left(2\theta_r - \frac{\pi}{3}\right)$$

$$x + y = 2A - 3L_{\Delta s}\left[\cos(2\theta_r) + \cos\left(2\theta_r - \frac{2}{3}\pi\right)\right] = 2A - 3L_{\Delta s}\left[2\cos\left(2\theta_r - \frac{\pi}{3}\right)\cos\left(\frac{\pi}{3}\right)\right] \quad (20)$$

$$x + y = 2A - 3L_{\Delta s}\cos\left(2\theta_r - \frac{\pi}{3}\right)$$

$$\tan\left(2\theta_r - \frac{\pi}{3}\right) = \frac{x - y}{\sqrt{3}(x + y - 2A)} \quad (21)$$

Then, the rotor position is obtained as follows:

$$\theta_r = \frac{1}{2}\tan^{-1}\left[\frac{x - y}{\sqrt{3}(x + y - 2A)}\right] + \frac{\pi}{6} \pm k\frac{\pi}{2} \quad (22)$$

Starting from the difference and sum of $y$ and $z$ it follows:

$$\theta_r = \frac{1}{2}\tan^{-1}\left[\frac{\sqrt{3}(z - x)}{(z + x - 2A)}\right] \pm k\frac{\pi}{2} \quad (23)$$

And starting from the difference and sum of $z$ and $x$:

$$\theta_r = \frac{1}{2}\tan^{-1}\left[\frac{y - z}{\sqrt{3}(y + z - 2A)}\right] - \frac{\pi}{6} \pm k\frac{\pi}{2} \quad (24)$$

with $k = 1,2,\dots,N$

These formulas allow for evaluating the initial rotor position with an uncertainty of ± 90°, which cannot be acceptable for vector control. The uncertainty can be solved by evaluating as a whole the values reached by the currents at the end of the application of the three feeding patterns (end of the first step).

If the highest value is reached at the end of feeding pattern "$a$-$b$", then the "$ab$" direction will have the minimum inductance; and the motor q-axis will be close to this direction. On the contrary, if this is the lowest value, the "$ab$" direction will have the maximum inductance; and the d-axis will be close to this direction. Repeating this assumption and considering the direction of space vector current during the different feedings, as shown in Fig. 8, the conditions to correct the angle are reported in Table I.

Since the estimated rotor position has an uncertainty of ± 90°, it is possible to add or subtract 90° to make it match one of the ranges previously shown. In this way, the rotor position can be obtained without uncertainty.

TABLE I
UNCERTAINTY ELIMINATION

| if | Is the highest | Is the lowest |
|---|---|---|
| $\bar{I}_{a,f}$ | $30° < \theta_r < 90°$ | $-60° < \theta_r < 0°$ |
| $\bar{I}_{b,f}$ | $-30° < \theta_r < 30°$ | $-90° < \theta_r < -60°$ ∨ $60° < \theta_r < 90°$ |
| $\bar{I}_{c,f}$ | $-90° < \theta_r < -30°$ | $0° < \theta_r < 60°$ |

where $\bar{I}_{a,f}$, $\bar{I}_{b,f}$, and $\bar{I}_{c,f}$ are the values of the currents at the end of the energization steps of the three feeding patterns. The coefficient 1.1 is used to avoid errors in the individuation of the sector due to measurement errors.

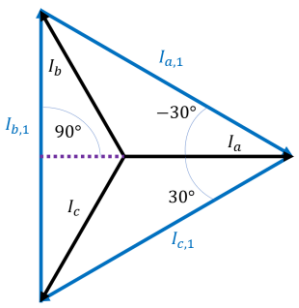


**Fig. 8.** Feeding pattern currents vector diagram and angles.

### C. Axis Inductances Estimation

Finally, it is possible to compute the direct and quadrature inductances according to:

$$L_d = L_{\sigma s} + \frac{3}{2}L_{\mu s} + \frac{3}{2}L_{\Delta s} = \frac{A}{2} - \frac{x-y}{2\sqrt{3}\,sin\left(2\theta_r - \frac{\pi}{3}\right)} \quad (25)$$

$$L_q = L_{\sigma s} + \frac{3}{2}L_{\mu s} - \frac{3}{2}L_{\Delta s} = \frac{A}{2} + \frac{x-y}{2\sqrt{3}\,sin\left(2\theta_r - \frac{\pi}{3}\right)} \quad (26)$$

The direct and quadrature inductance, together with the phase resistance, are useful for a good sizing of the gains of the PI current regulator for the best dynamic behavior.

### D. PI current regulator parameter

For the PI current regulator parameter it is possible to apply the well-known expressions which correlate the motor parameters (axes inductances and resistance) to the proportional and integrator coefficients of the PI, [44]-[45]. For the sake of clarity the expressions has been reported.

$$T_{Nd} = \tau_d = \frac{L_d}{R_s} \qquad T_{Nq} = \tau_q = \frac{L_q}{R_s} \quad (27)$$

$$T_I = 2\frac{K_{cm}}{R_s}T_{cm} \qquad T_{cm} = \alpha\frac{1}{2}T_{pwm} \quad (28)$$

$$k_{Pd} = \frac{T_{Nd}}{T_I} \qquad k_{Pq} = \frac{T_{Ndq}}{T_I} \qquad k_I = \frac{1}{T_{I(dq)}} \quad (29)$$

where $\tau_d$ and $\tau_d$ are the time constants of the *d-q* axes, $T_{Nd}$, $T_{Nq}$, and $T_{I(dq)}$ are time constants of the proportional and integral components of the *d-q* regulators, $K_{cm}$ and $T_{cm}$ are the equivalent gain and time constant of the power electronics, $T_{pwm}$=100 μs is the PWM period, $\alpha$ is a design coefficient for the current regulators, and $k_{Pd}$, $k_{Pd}$,and $k_I$ are the *d-q* axes proportional and integral gains, respectively.

After the computation of all these parameters, including the initial position discussed in the previous subsection, it is possible to start the motor control.

## IV. Additional effects

The adopted expressions neglect nonlinear effects due to the saturation, cross-coupling, and bus voltage variation. These effects and their possible impact in the estimation of the parameters are discussed in this section.

The ribs in the SynRel reach saturation also with a low flux level modifying the current behavior; therefore, a nonlinear effect with the modification of the inductance can be seen during the supply. In particular, when the feeding pattern is close to the q-axis, it is possible to verify a quick saturation of the radial ribs with a nonlinear behavior of the current. Because of the non-linearity affecting the current shape, the time window and the considered starting instant in which the derivative is computed affect the estimation of the position; when this saturation occurs, it is not possible to select the first instants for the position estimation because the inductance parameters are not constant.

Even if the patterns supply only two phases, the current could also flow in the third one. This is caused by the fact that the potential of the star center exceeds the values of the DC rails and the "third phase" (which normally should not be energized) is subject to a re-circulation. This phenomenon depends on the rotor position through the anisotropy component of the phase voltages (see eqs. .(1) to (3)): the unbalance between the voltages of the fed phases produces this effect. Therefore, the current can flow through the inverter diodes depending on the rotor position and the feeding pattern. This anomaly might damage the entire procedure for the initial position estimation because, in the computation, the current in the "third phase" was considered equal to zero.

A way to prevent the calculation from being affected by this phenomenon is to limit the derivative measurement to a time when the current in the open phase is zero.

Another effect that was not considered in the previous section is the variation of the DC voltage due to the inductance energy transferred to the capacitor. This happens when all the switch commands are set to 0. Therefore, for the computation of the phase resistance, further consideration arises. In the computation of the phase resistance, the DC bus voltage values during the energization and de-energization steps are supposed to be constant and equal. Hence, considering the current behavior quite linear in the first transient instants (motor fed with the maximum voltage), the value of the $I_2(t)$ linearly depends on the DC bus voltage so that it can be modified according to:

$$\widetilde{I_2}(t) = I_2(t) + I_2(0)\left(\frac{\bar{V}_{dc}}{V_{dc}} - 1\right)\frac{t}{t_a} \quad (30)$$

where $\widetilde{I_2}(t)$ is the new value for the computation of the phase resistance, $\bar{V}_{dc}$ is the mean value of the DC bus voltage during the de-energization, and $t_a$ is the duration of the de-energization operation.

## V. Simulation Results

The expressions deduced in the previous sections refer to a magnetically linear model of the SynRel. A Finite Elements (FE) motor model allowed us to verify its effectiveness. Using the FE model, all the non-linearity effects of the machine, such as cross-coupling and saturation, are taken into account.

The Ansys/Maxwell software package has been used. It allowed the joining Finite Elements (FE) analysis of the electric motor and the dynamic simulation of the feeding power electronics and control, namely "co-simulation" [46]. A 4-poles, 4-kW motor, available in the lab for experimental validations, has been considered.

The simulation implements the technique explained in the previous section to feed the motor. The three energization steps of the feeding patterns are imposed for a time span of 1.5 ms, while the de-energization step is maintained for 4 ms. The motor mesh used in the software, such as the machine geometry, is shown in Fig. 9, while the main motor data and parameters are listed in Table II. Once the machine model has been created, the co-simulation is carried out by interfacing the motor model with a simplified voltage source inverter and simulating the identification procedure.

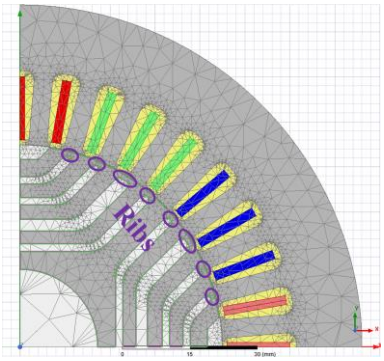


**Fig. 9.** Motor shape and its FE mesh.

TABLE II
MAIN DATA OF THE SYNREL MOTOR

| **Values @ rated operating condition** | |
|---|---|
| Phase voltage | $\hat{V}_n = 220 \times \sqrt{2}\ V$ |
| Phase current | $\hat{I}_n = 10.67\ A$ |
| Speed | $n_n = 1500\ rpm$ |
| Torque | $T_{en} = 20\ Nm$ |
| **Parameters** | |
| Direct inductance | $L_d = 186\ mH$ |
| Quadrature inductance | $L_q = 34.1\ mH$ |
| Phase resistance | $R_s = 1.975\Omega\ @20°C$ |

The simulation implements a one-quadrant supply: hence, the voltage and the power supply's current are always positive.

Fig. 10 shows the results regarding the phase currents when the rotor is aligned with the phase "$a$" with the proposed supply pattern shown in Fig. 2 and Fig. 3 ("a-b"), Fig. 4 ("b-c"), and Fig. 5 ("c-a"). The strongly non-linear behavior of the currents of the phase "$b$" and "$c$" when the feeding pattern "$b$-$c$" is applied can be explained by the quick saturation of the ribs (as explained in the previous section) due to the quadrature of the applied current space vector with respect to the rotor position; hence the "$b$-$c$" is close to the $q$-axis.

Thus, the position estimation procedure needs to be studied by evaluating several time windows. In facts, the saturation of the ribs can affect the estimation since it happens differently for each of the three feeding patterns because it depends on the rotor position and current space vector angle.

Fig. 11 and Fig. 12 show the current profiles with the position equal to 135° and 90°, respectively. In both cases, it can be noticed that, during the feeding period, the current flows in all three phases. As discussed in the previous section, the derivative measurement should be limited to a time windows in which the current in the open phase is zero.

The method requires the values of the derivative of the currents. The Ordinary Least Squares (OLS) algorithm is considered to minimize the error due to the non-linearity of the current and the error measurement. Also noise effects can be reduced considering a sufficient number of points for the derivative computation. The algorithm finds the linear approximation whose slope is the desired value, given the considered time interval and measured data.

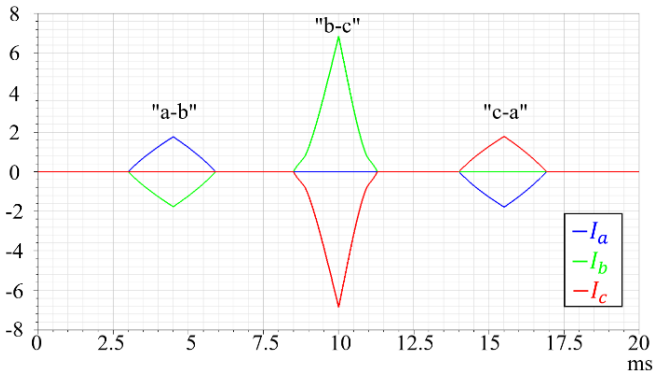


**Fig. 10.** Behavior of the phase currents with a position of 0°.

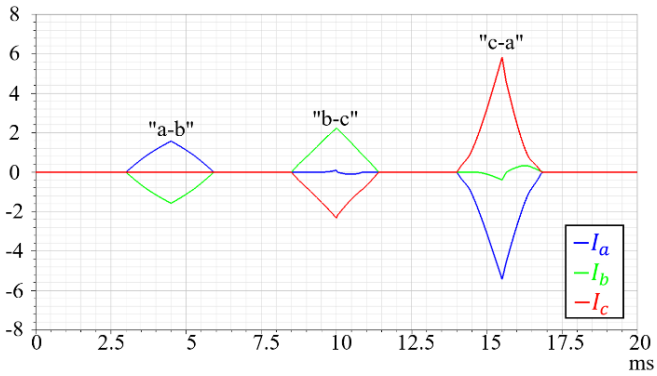


**Fig. 11.** Behavior of the phase currents with a position of 135°.

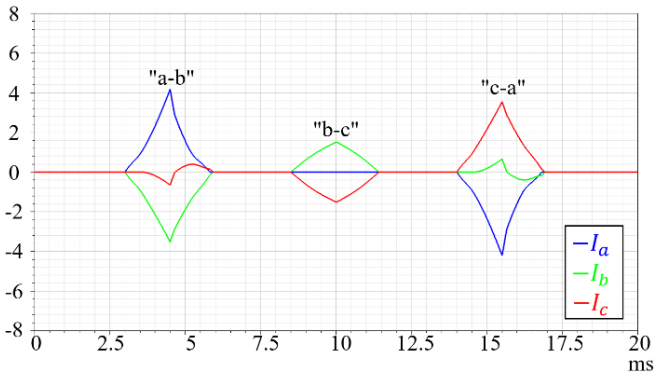


**Fig. 12.** Behavior of the phase currents with a position of 90°.

A first shrewdness could be to consider only the first instants of the current growth in the three cases, assuming that the saturation does not have a significant role when low current values are involved. But, if only the first instants of current rising were used, the estimation of the current derivative would not be reliable because of the low number of points involved in the calculation. In order to correctly calculate the derivative, it is necessary to wait until the ribs are saturated and then complete the calculation. It is all about reaching a proper compromise between a good estimation of the current derivative and the possibility of having a constant inductance in the range in which the current is analyzed. For this reason, a parametric study has been conducted by varying both the time window and the instant for the calculation of the derivates.

Fig. 13 shows the position estimation error achieved by the proposed method as a function of the actual rotor position,

using different time windows and different instants to calculate the phase current derivatives.

Despite the eqs. (7) and (8) are exponentially increasing and decreasing this is not visible in the results. This is due to the maximum current value that the motor should reach with the applied DC voltage. Considering that in steady-state at a standstill, the only term is the resistive one, the maximum current is much over than the one that has been reached in simulation (this condition is always true) and what is shown in the simulation is the first part of the exponential curve which is quite linear. The only deformation that can be found is due to the variation of the $q$-axis inductance caused by the ribs saturation. The same considerations can be done in the next section in which the experimental results are presented. When the current is applied in the $d$-direction ("a-b" in Fig. 10), the maximum value reached is under 2 A, far away from the saturation condition (around 4 A). It is not necessary to investigate high current levels because it is possible to tune the PI current regulator in the linear part of the inductance by having a good match in that area. In saturation conditions, there is not a perfect tuning, but the variation of the inductance (if a very deep saturation is reached) is not so large, however allowing a good current control. If the application requires a strong overload condition (very high saturation), the PI coefficients computed with the estimated inductance could lead to poor controllability of the machine. This could be partially compensated with a small reduction of the direct axis inductance value in the computation of PI current coefficients.

Fig. 13 presents just the more significant points, analyzed in different conditions: the curve "first instants" corresponds to the application of the procedure for the rotor position estimation at the start of step 1 and a time window that maintains a linear behavior of the current; the curve "last instant" is achieved by applying the procedure for the rotor position estimation at the end of step 1 and a time window that guarantees a linear behavior of the current; the curve "in the middle" means to use the average value of the current and its derivative computed in the above two methods; finally the curve "best conditions" considers the larger time window in which the current has a linear behavior considering the three feeding patterns. In all the cases, the error remains limited to a maximum of 4°, making the method reliable even in different operating conditions. In the best conditions, the maximum error is around 1°.

As described, in addition to the computation of the initial position, the estimation procedure is able to calculate the phase resistance and the $d$-$q$ axes inductances. Table III reports the values achieved compared to those respectively set (phase resistance) or extracted (axis inductances) by the FE model. The value of the estimated phase resistance is slightly higher than the (rated) one used in the FEA; this difference is due to the equivalent resistance of the diodes and switches in series with the resistance of the motor (in the simulation, supposed equal to 0.1 Ω).

The error on the calculation of the initial position, if minor, can be recovered if sensorless control is used or nullified with an incremental position sensor with zero pulse signal. However, if the application requires the exact value of the initial position, it is possible to align the rotor using a current space vector with the same direction of the estimated 8sitionn, thus reducing the rotor motion (equal to the angle error) and guaranteeing extact value of the initial position. Another strategy, useful in all those applications in which the rotor can turn in one direction only, consists of an alignment according to a position that will surely make the rotor rotate in the wanted direction.

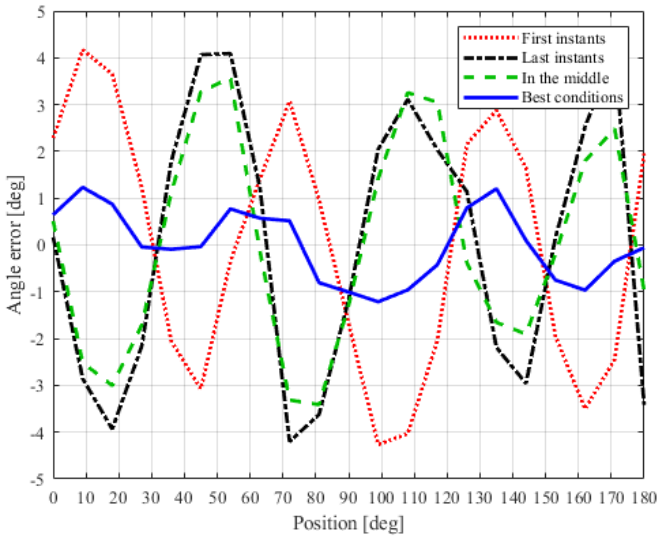


**Fig. 13.** Error between the estimated position and the real one with different time windows and starting instants (co-simulation).

TABLE III
MAIN DATA OF THE SYNREL MOTOR

| Parameter | FEA | Estimated |
|---|---|---|
| direct inductance ($L_d$) | 186 $mH$ | 187.8 $mH$ |
| quadrature inductance ($L_q$) | 34.1 $mH$ | 34.7 $mH$ |
| phase resistance ($R_s$) | 1.975 Ω | 2.09 Ω |

## VI. EXPERIMENTAL RESULTS

The experimental set-up consists of a one-quadrant power supply, an IGBT inverter that operates at 10 kHz PWM frequency, and control made through a microcontroller TMS 320C28335. This drive feeds the synchronous reluctance motor with four poles and four flux barriers on the rotor presented in Section V and shown in Fig. 14.

The experimental tests have been performed similarly to the simulations presented in the previous section. Hence the same time windows have been considered, and the same feeding patterns mentioned in Section II have been used. Moreover, all the experiences were carried out with a "cold" motor so that the winding temperature was close to the reference value for resistance measurement (see Table III).

Fig. 15, Fig. 16, and Fig. 17 show the phase current responses obtained for different rotor position values in the

same condition of the simulation results (Fig. 10, Fig. 11, and Fig. 12). The behaviors are very similar to those presented in the previous section. The results given by the simulations are consistent with the experimental tests. Minor differences can be because of the deviation of magnetic properties due to manufacturing, end winding effects not taken into account in the 2D simulations, and manufacturing tolerances in stator and rotor cores.

Also, in this case, the maximum current in the $d$-direction is lower than 2 A, but as mentioned, this does not affect the results in terms of position, phase resistance, and axes inductances estimation. The parameters computed with this current level correctly estimate the machine in an unsaturated condition which is the most frequent operating area (low and medium torque).

As done for the simulation study, the experimental position estimation error has been evaluated with different settings of the identification procedure. Fig. 18 shows its trend in the same conditions of the time window and starting point for calculating the current derivative considered in the simulation study.

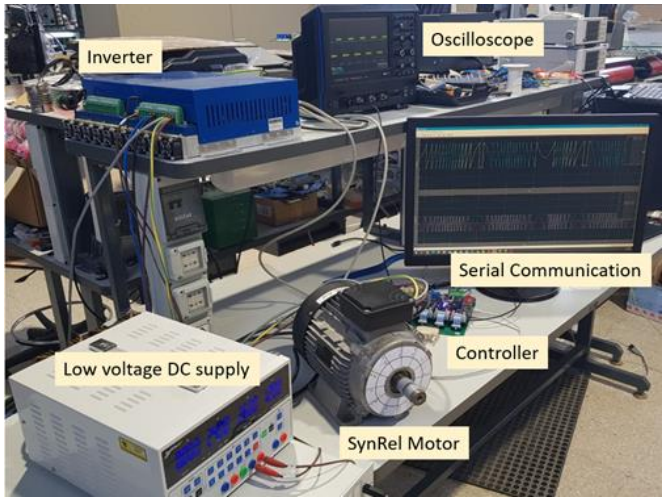


**Fig. 14.** Motor test bench (left) and drive system (right).

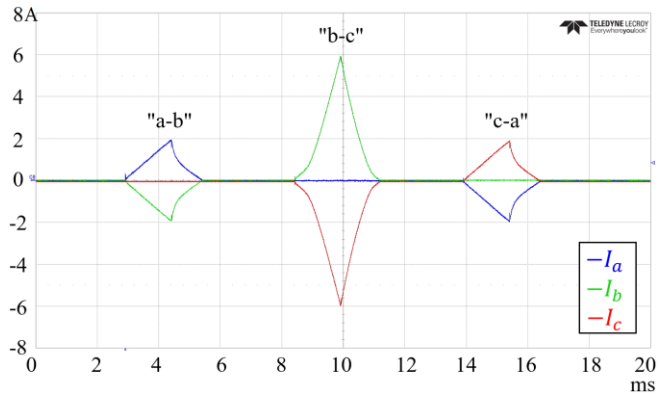


**Fig. 15.** Behavior of the phase currents with a position of 0°.

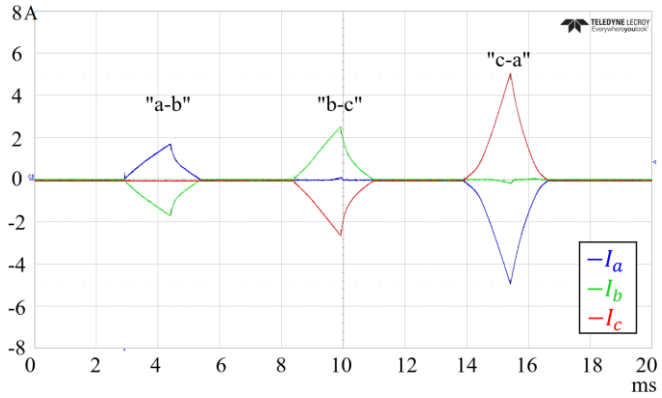


**Fig. 16.** Behavior of the phase currents with a position of 135°.

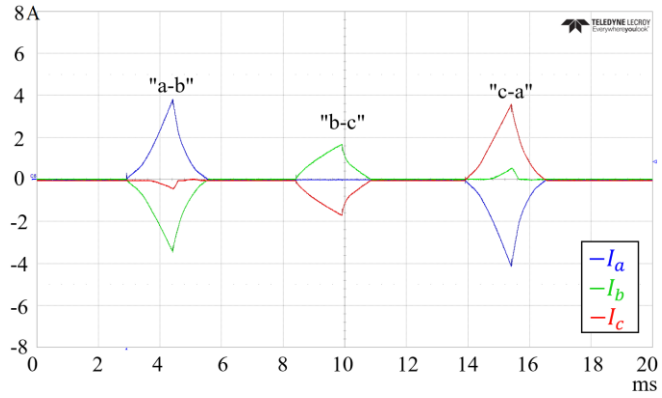


**Fig. 17.** Behavior of the phase currents with a position of 90°.

The experimental results are computed in the same conditions of co-simulation. The errors obtained in the experimental results, obtained in the different curves, are slightly higher than those of the co-simulation. However, in the "best conditions", described in the previous section, the maximum error is under 4 degrees. Still, either way, their values justify the utilization of this method for the initial position estimation.

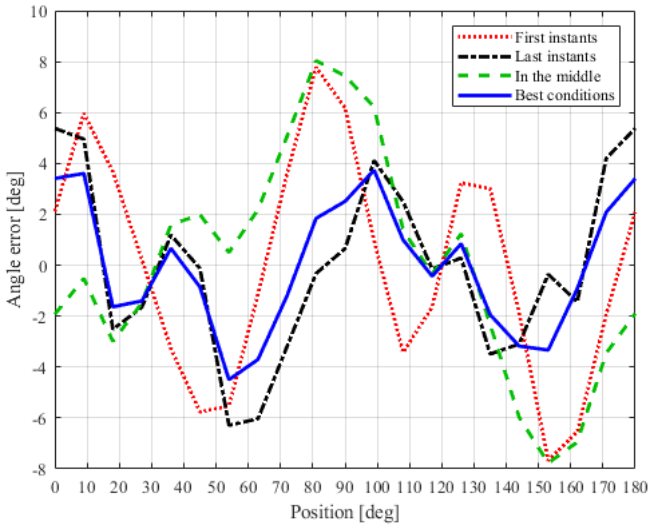


**Fig. 18.** Experimental error between the estimated position and the real one with different time windows.

Finally, the experimentally estimated phase resistance and axis inductances are reported in Table IV, compared to those achieved in co-simulation and those provided by the FEA. In this case, the difference between the experimentally estimated phase resistance and the measured one used in the FEA is higher: this is probably due to the higher equivalent resistance of the power supply.

TABLE IV
EXPERIMENTAL RESULTS OF PARAMETER ESTIMATION

| Parameter | FEA | Estimated (simulation) | Estimated (experimental) | Measured |
|---|---|---|---|---|
| $L_d$ | 186 $mH$ | 187.8 $mH$ | 191.5 $mH$ | 189.3 $mH$ |
| $L_q$ | 34.1 $mH$ | 34.7 $mH$ | 38.6 $mH$ | 37.1 $mH$ |
| $R_s$ | 1.975 Ω | 2.09 Ω | 2.18 Ω | 1.975 Ω |
| $k_{Pd}$ | 1860 Ω | 1878 Ω | 1915 Ω | 1893 Ω |
| $k_{Pq}$ | 341 Ω | 347 Ω | 386 Ω | 371 Ω |
| $k_I$ | 19750H | 20900 H | 21800 H | 19750H |

## VII. CONCLUSION

This paper proposes a new unified approach for the commissioning of SynRel motor drives, which allows for identifying the phase resistance, the axes inductances, and the starting rotor position.

The approach exploits the flux model of the machine and an original pattern of feeding voltage. The method is general, can be implemented with standard control hardware, and applies to all the synchronous reluctance machines.

The obtained results prove the effectiveness of the proposal. The estimation errors range in a few percent for both the initial position and the values of the parameters. The identification is satisfactory in all the analyzed rotor positions and with different choices of the measurement time windows during the feeding patterns, which testifies the method's robustness.

Ultimately, the estimation method proposed in this paper is the kernel for the fast commissioning of SynRel motor drives. The estimated motor parameters allow the setting up of the current control regulators. The estimated rotor position can also be used to achieve a "soft" alignment (with minimum movement) or a "safe" alignment in the wanted direction for applications in which there is such a requirement. Compared to the typically embedded one, the main advantage of the proposed method is the short feeding time, which leads to minimal movement even in no-load conditions.

Future work is to remove the simplifying modeling assumptions considered in this paper to have a more accurate representation of the machine and improve the estimates.

## REFERENCES

[1] A. Credo, F. Parasiliti Collazzo, M. Tursini and M. Villani, "A Fast Estimation of the Initial Rotor Position of Synchronous Reluctance Motors," *2022 International Conference on Electrical Machines (ICEM)*, 2022, pp. 1471-1476.

[2] I. Boldea, L. Tutelea, L. Parsa and D. Dorrell, "Automotive electric propulsion systems with reduced or no permanent magnets: An overview," *IEEE Trans. Ind. Electron.*, vol. 61, no. 10, pp. 5696-5711, 2014.

[3] M. Murataliyev, M. Degano, M. Di Nardo, N. Bianchi and C. Gerada, "Synchronous Reluctance Machines: A Comprehensive Review and Technology Comparison," in *Proceedings of the IEEE*, vol. 110, no. 3, pp. 382-399, March 2022.

[4] "Rare Earth Free e-drives featuring low-cost manufacturing" *RefreeDrive*, 2021 [Online]. Available: www.refreedrive.eu

[5] A. Credo, M. Villani, M. Popescu and N. Riviere, "Application of Epoxy Resin in Synchronous Reluctance Motors With Fluid-Shaped Barriers for E-Mobility," in IEEE Transactions on Industry Applications, vol. 57, no. 6, pp. 6440-6452, Nov.-Dec. 2021.

[6] N. Bianchi, S. Bolognani, E. Carraro, M. Castiello and E. Fornasiero, "Electric Vehicle Traction Based on Synchronous Reluctance Motors," *IEEE Trans. On Ind. Appl.*, vol. 52, no. 6, pp. 4762-4769, 2016.

[7] Y. Wang, D. Ionel, V. Rallabandi, M. Jiang and S. Stretz, "Large-Scale Optimization of Synchronous Reluctance Machines Using CE-FEA and Differential Evolution," *IEEE Trans. On Ind. Appl.*, vol. 52, no. 6, pp. 4699-4709, 2016.

[8] E. Howard, M.J. Kamper, S. Gerber, "Asymmetric flux barrier and skew design optimization of reluctance synchronous machines," *IEEE Trans. Ind. Appl.*, vol. 51, issue 5, pp. 3751-3760, 2015.

[9] A. Credo, G. Fabri, M. Villani, and M. Popescu, "A Robust Design Methodology for Synchronous Reluctance Motors," in *IEEE Transactions on Energy Conversion*, vol. 35, no. 4, pp. 2095-2105, Dec. 2020.

[10] Y. Wang, D. Ionel, V. Rallabandi, M. Jiang and S. Stretz, "Large-Scale Optimization of Synchronous Reluctance Machines Using CE-FEA and Differential Evolution," *IEEE Trans. On Ind. Appl.*, vol. 52, no. 6, pp. 4699-4709, 2016.

[11] A. Credo, A. Cristofari, S. Lucidi, F. Rinaldi, F. Romito, M. Santececca, M. Villani, "Design Optimization of Synchronous Reluctance Motor for Low Torque Ripple," *AIRO Springer Series*, pp. 53-69, 2019.

[12] G. Pellegrino, F. Cupertino, and C. Gerada, "Automatic design of synchronous reluctance motors focusing on barrier shape optimization," *IEEE Trans. Ind. Appl.*, vol. 51, no. 2, pp. 1465-1474, 2015.

[13] A. Yousefi-Talouki, P. Pescetto, G. Pellegrino and I. Boldea, "Combined Active Flux and High-Frequency Injection Methods for Sensorless Direct-Flux Vector Control of Synchronous Reluctance Machines," in *IEEE Transactions on Power Electronics*, vol. 33, no. 3, pp. 2447-2457, March 2018.

[14] A. Yousefi-Talouki, P. Pescetto, and G. Pellegrino, "Sensorless Direct Flux Vector Control of Synchronous Reluctance Motors Including Standstill, MTPA, and Flux Weakening," in *IEEE Transactions on Industry Applications*, vol. 53, no. 4, pp. 3598-3608, July-Aug. 2017.

[15] M. Hinkkanen, P. Pescetto, E. Mölsä, S. E. Saarakkala, G. Pellegrino, and R. Bojoi, "Sensorless Self-Commissioning of Synchronous Reluctance Motors at Standstill Without Rotor Locking," in *IEEE Transactions on Industry Applications*, vol. 53, no. 3, pp. 2120-2129, May-June 2017.

[16] P. Pescetto and G. Pellegrino, "Sensorless magnetic model and pm flux identification of synchronous drives at standstill," *2017 IEEE International Symposium on Sensorless Control for Electrical Drives (SLED)*, Catania, 2017, pp. 79-84.

[17] C. Li, G. Wang, G. Zhang, N. Zhao, and D. Xu, "Review of parameter identification and sensorless control methods for synchronous reluctance machines," in *Chinese Journal of Electrical Engineering*, vol. 6, no. 2, pp. 7-18, June 2020.

[18] R. Dutta and M. F. Rahman, "A Comparative Analysis of Two Test Methods of Measuring d- and q-Axes Inductances of Interior Permanent-Magnet Machine," in *IEEE Transactions on Magnetics*, vol. 42, no. 11, pp. 3712-3718, Nov. 2006.

[19] M. A. Jabbar, J. Dong, and Z. Liu, "Determination of machine parameters for internal permanent magnet synchronous motors," *Second International Conference on Power Electronics, Machines and Drives (PEMD 2004)*, 2004, pp. 805-810 Vol.2.

[20] H. Zhaobin, Y. Linru, and W. Zhaodong, "Sensorless initial rotor position identification for non-salient permanent magnet synchronous motors based on dynamic reluctance difference," *IET Power Electronics*, vol. 7, no. 9, pp. 2336-2346, 2014.

[21] F. Parasiliti, R. Petrella, M. Tursini, "Initial Rotor Position Estimation Method for PM Motors," IEEE Trans. On Industry Applications, vol. 39, no. 6, pp.1630-1640, Nov/Dec 2003.

[22] Y. Wang et al., "Initial Rotor Position and Magnetic Polarity Identification of PM Synchronous Machine Based on Nonlinear Machine Model and Finite Element Analysis," *IEEE Transactions on Magnetics*, vol. 46, no. 6, pp. 2016-2019, 2010.

[23] H. -C. Yeh and S. -M. Yang, "Phase Inductance and Rotor Position Estimation for Sensorless Permanent Magnet Synchronous Machine Drives at Standstill," in *IEEE Access*, vol. 9, pp. 32897-32907, 2021.

[24] X. Wu *et al*., "Initial Rotor Position Detection for Sensorless Interior PMSM With Square-Wave Voltage Injection," in *IEEE Transactions on Magnetics*, vol. 53, no. 11, pp. 1-4, Nov. 2017, Art no. 8112104.

[25] X. Jin, R. Ni, W. Chen, F. Blaabjerg and D. Xu, "High-Frequency Voltage-Injection Methods and Observer Design for Initial Position Detection of Permanent Magnet Synchronous Machines," in *IEEE Transactions on Power Electronics*, vol. 33, no. 9, pp. 7971-7979, Sept. 2018.

[26] K. Lin, P. Wang, P. Cai, X. Wu and M. Lin, "Fast Initial Rotor Position Estimation for IPMSM with Unipolar Sequence-Pulse Injection," in *IEEE Transactions on Energy Conversion*.

[27] S. Li, S. Zheng, X. Zhou, and J. Fang, "A Novel Initial Rotor Position Estimation Method at Standstill for Doubly Salient Permanent Magnet Motor," in *IEEE Transactions on Industrial Informatics*, vol. 14, no. 7, pp. 2914-2924, July 2018.

[28] Y. Cai, Y. Wang, H. Xu, S. Sun, C. Wang and L. Sun, "Research on Rotor Position Model for Switched Reluctance Motor Using Neural Network," in *IEEE/ASME Transactions on Mechatronics*, vol. 23, no. 6, pp. 2762-2773, Dec. 2018.

[29] L. Ge, H. Xu, Z. Guo, S. Song, and R. W. De Doncker, "An Optimization-Based Initial Position Estimation Method for Switched Reluctance Machines," in *IEEE Transactions on Power Electronics*, vol. 36, no. 11, pp. 13285-13292, Nov. 2021.

[30] K. R. Geldhof, A. P. M. Van den Bossche and J. A. Melkebeek, "Rotor-Position Estimation of Switched Reluctance Motors Based on Damped Voltage Resonance," in *IEEE Transactions on Industrial Electronics*, vol. 57, no. 9, pp. 2954-2960, Sept. 2010.

[31] D. Raca, P. Garcia, D. Reigosa, F. Briz and R. Lorenz, "Carrier-Signal Selection for Sensorless Control of PM Synchronous Machines at Zero and Very Low Speeds," *IEEE Transactions on Industry Applications*, vol. 46, no. 1, pp. 167-178, 2010.

[32] Z. Zhu and L. Gong, "Investigation of Effectiveness of Sensorless Operation in Carrier-Signal-Injection-Based Sensorless-Control Methods," *IEEE Trans. On Ind. Electron.*, vol. 58, no. 8, pp. 3431-3439, 2011.

[33] J. Sun, J. Zhao, L. Tian, Y. Song and Y. Liu, "Bandwidth and Audible Noise Improvement of Sensorless IPMSM Drives Based on Amplitude Modulation Multirandom Frequency Injection," in *IEEE Transactions on Power Electronics*, vol. 37, no. 12, pp. 14126-14140, Dec. 2022.

[34] S. -C. Agarlita, I. Boldea and F. Blaabjerg, "High-Frequency-Injection-Assisted "Active-Flux"-Based Sensorless Vector Control of Reluctance Synchronous Motors, With Experiments From Zero Speed," in *IEEE Transactions on Industry Applications*, vol. 48, no. 6, pp. 1931-1939, Nov.-Dec. 2012

[35] A. Varatharajan and G. Pellegrino, "Sensorless Control of Synchronous Reluctance Motor Drives: Improved Modeling and Analysis Beyond Active Flux," *2019 IEEE International Electric Machines & Drives Conference (IEMDC)*, San Diego, CA, USA, 2019, pp. 419-426

[36] M. Laumann, C. Weiner and R. M. Kennel, "Convergence Investigation of Injection-Based Encoderless Control Algorithms for RSMs in Deep Magnetic Saturation," in *IEEE Access*, vol. 10, pp. 30091-30108, 2022

[37] S. Bolognani, L. Peretti, M. Zigliotto and E. Bertotto, "Commissioning of Electromechanical Conversion Models for High Dynamic PMSM Drives," in *IEEE Transactions on Industrial Electronics*, vol. 57, no. 3, pp. 986-993, March 2010.

[38] A. Uphues, K. Nötzold, R. Wegener and S. Soter, "Comparison of parameter identification approaches with linearised process models based on RLS for induction machines with P > 100 kW," *2016 IEEE International Conference on Industrial Technology (ICIT)*, Taipei, Taiwan, 2016, pp. 134-140.

[39] S. Sheng, X. Cheng, H. Lu, W. Qu and Y. Li, "An accurate rotor time constant estimation method for self-commissioning of multi-scale induction motor drives," *2011 IEEE Energy Conversion Congress and Exposition*, 2011, pp. 1700-1707.

[40] S. Peresada, S. Kovbasa, D. Prystupa and S. E. Lyshevski, "Identification of induction motor parameters for self-commissioning procedure: A new algorithm and experimental verification," *2014 IEEE 23rd International Symposium on Industrial Electronics (ISIE)*, 2014, pp. 818-823.

[41] P. G. Carlet, F. Tinazzi, S. Bolognani, and M. Zigliotto, "An Effective Model-Free Predictive Current Control for Synchronous Reluctance Motor Drives," in *IEEE Transactions on Industry Applications*, vol. 55, no. 4, pp. 3781-3790, July-Aug. 2019.

[42] C. Lin, J. Yu, Y. Lai and H. Yu, "Improved Model-Free Predictive Current Control for Synchronous Reluctance Motor Drives," in *IEEE Transactions on Industrial Electronics*, vol. 63, no. 6, pp. 3942-3953, June 2016.

[43] H. Mesai-Ahmed, I. Jlassi, A. J. Marques Cardoso and A. Bentaallah, "Model-Free Predictive Current Control of Synchronous Reluctance Motors Based on a Recurrent Neural Network," in *IEEE Transactions on Industrial Electronics.*

[44] Bühler Hansruedi, *Electronique de réglage et de Commande*. Lausanne: Presses Polytechniques et Universitaires Romandes, 1990.

[45] W. Leonhard, *Control of electrical drives*. Berlin: Springer Berlin, 2013.

[46] L. Di Leonardo, M. Popescu, M. Tursini and M. Villani, "Finite Elements Model Co-Simulation of an Induction Motor Drive for Traction Application," *IECON 2019 - 45th Annual Conference of the IEEE Industrial Electronics Society*, 2019, pp. 1059-1065.

[47] M. Tursini, M. Villani, G. Fabri, A. Credo, F. Parasiliti and A. Abdelli, "Synchronous Reluctance Motor: Design, Optimization, and Validation," *2018 International Symposium on Power Electronics, Electrical Drives, Automation and Motion (SPEEDAM)*, Amalfi, 2018, pp. 1297-1302

## APPENDIX – EXPRESSION OF SELF AND MUTUAL INDUCTANCES, FLUX LINKAGES, AND VOLTAGES

$$L_{aa} = L_{\sigma s} + L_{\mu s} + L_{\Delta s}\cos(2\theta_r)$$

$$L_{bb} = L_{\sigma s} + L_{\mu s} + L_{\Delta s}\cos(2\theta_r + 2/3\pi)$$

$$L_{cc} = L_{\sigma s} + L_{\mu s} + L_{\Delta s}\cos(2\theta_r - 2/3\pi)$$

$$L_{ab} = L_{ba} = -1/2\, L_{\mu s} + L_{\Delta s}\cos(2\theta_r - 2/3\pi)$$

$$L_{bc} = L_{cb} = -1/2\, L_{\mu s} + L_{\Delta s}\cos(2\theta_r)$$

$$\varphi_a = L_{aa}I_a + L_{ab}I_b + L_{ac}I_c$$

$$\varphi_b = L_{ba}I_a + L_{bb}I_b + L_{bc}I_c$$

$$\varphi_c = L_{ca}I_a + L_{cb}I_b + L_{cc}I_c$$

$$V_a = R_s I_a + d\varphi_a/dt$$

$$V_b = R_s I_b + d\varphi_b/dt$$

$$V_c = R_s I_c + d\varphi_c/dt$$